Supporting Information for

Influence of Discrete Defects on Observed Acoustic-Phonon Dynamics in Layered Materials Probed with Ultrafast Electron Microscopy

Spencer A. Reisbick, Yichao Zhang, and David J. Flannigan*

Department of Chemical Engineering and Materials Science, University of Minnesota, 421 Washington Ave. SE, Minneapolis, Minnesota 55455, United States

*Author to whom correspondence should be addressed.
Email: flan0076@umn.edu
Office: 612-625-3867
Fax: 612-626-7246

The Supporting Information includes:

Supporting videos 1-3
Supporting video captions
Materials and Methods
Figures S1-S6

Video Captions

Supporting Video 1. UEM bright-field video of basal-plane acoustic-phonon dynamics in 1T-TaS_2. Direct imaging of basal-plane acoustic-phonon propagation in multilayer TaS_2. Individual image acquisition time was 30 s, and the UEM image scan ranged from -100 ps to 400 ps. Variable time steps were used.

Supporting Video 2. UEM bright-field video of *c*-axis acoustic-phonon dynamics in 1T-TaS_2. Direct imaging of *c*-axis acoustic-phonon oscillations in multilayer TaS_2. Individual image acquisition time was 5 s, and the UEM image scan ranged from -50 ps to 350 ps. Time steps of 1 ps were used.

Supporting Video 3. Spatial frequency map generated from the UEM image series shown in Supporting Video 2. False-colored frequency map generated from a pixel-by-pixel analysis of the UEM temporal image series shown in Supporting Video 2. The video spans from 0 GHz to 93.4 GHz at 0.6-GHz steps. The intensity of each pixel is the magnitude of the FFT signal at the frequency indicated in each frame. White and red pixels indicate high and low signal intensities, respectively. High-intensity images at low frequencies (*i.e.*, the first three to four images) correspond to the difference in background intensity change over the course of the experiment.

Materials and Methods

Determination of basal-plane acoustic-phonon velocity for the specimen in Figure 1.

Figure S1 summarizes the image-analysis method used to determine the basal-plane acoustic-phonon velocity from a UEM ps bright-field image series. Figure S1a contains a select UEM image of the TaS_2 specimen highlighted in Figure 1 and in Supporting Video 1, while Figure S1b shows a typical space-time contour plot (STCP) generated from the UEM image series. Here, an ROI measuring 800-nm long was selected for the analysis; propagating phonons are observed moving across this specimen region and parallel to the length of this ROI in the UEM image series. The ROI width was set at 7 pixels in order to increase the signal-to-noise ratio of the resulting individual spatiotemporal slices while still spatially isolating the pertinent contrast dynamics. A single wavefront appears as a dark, linear band in the STCP and directly returns the direction, speed, and temporal dispersion behaviors. As has been observed with other TMDs using this method, the velocity of each wavefront is fixed to approximately the bulk speed of sound without any apparent dispersion over time.[1-4] Velocity for an individual phonon wavefront is determined by fitting sections of the band in the STCP to a peak function (*e.g.*, Gaussian) and then plotting the temporal peak position as a function of position within the ROI (Figure S1c). Here, the speed was found to be 4.2 ± 0.2 nm/ps.

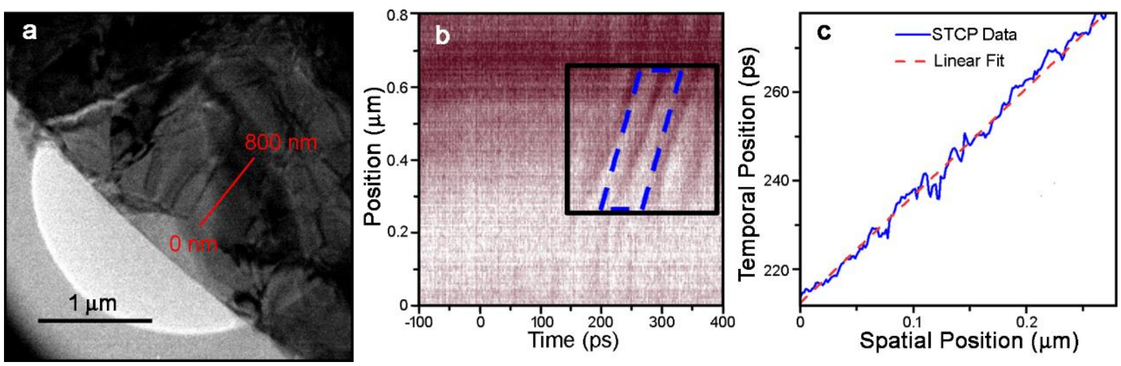

Figure S1. Determination of basal-plane acoustic-phonon velocities *via* generation and analysis of space-time contour plots (STCPs) from UEM image series. (a) Select UEM image of multilayer TaS_2 highlighting the position and length of an 800-nm ROI from which the analysis was performed. The TaS_2 flake is mounted on a holey-carbon support. (b) STCP generated from the ROI shown in (a). The blue dashed parallelogram highlights the region used to fit sections of the phonon wavefront band from which velocity information is extracted. The sign of the slope indicates the in-plane direction is away from the vacuum-crystal interface. (c) Plot of the temporal peak positions from fitting the band in (b) to peak functions along the position of the ROI. The red dashed line is a least-squares fit to the data and returns (upon inversion) the wavefront speed (here, 4.2 ± 0.2 nm/ps).

Determination of the BF1 and BF2 spots and the crystal terrace position in Figures 2 and 3.

The BF1 and BF2 spots in Figure 2a and Figure 3 were spatially positioned onto the first UEM image using Hough transform edge detection. A HAADF-STEM image was used to identify the terrace and to corroborate the thickness measured with EELS. A thermionic image containing the selected-area aperture used in the UEM SAED measurement was acquired following the completion of the diffraction scan. The analysis regions and FFT map were determined from the UEM image series, so no additional correlation was necessary. Figure S3 shows a schematic of the Hough transform method used. For each Hough transform, the raw micrograph was converted into a binary image using edge detection *via* the Canny method. Once the binary image was created, the Hough transform was performed using 0.5° steps and a radial resolution of 0.5 pixels. The exact peak position was identified as the maximum-amplitude pixel in the narrowest band of the intersection in each transform. In most instances, this peak was also the local maximum. However, some edges contain slight bends, which broaden the Hough signal. The polar coordinates corresponding to each edge were converted to Cartesian coordinates, and the new formulae were used to match features within each image to one another.

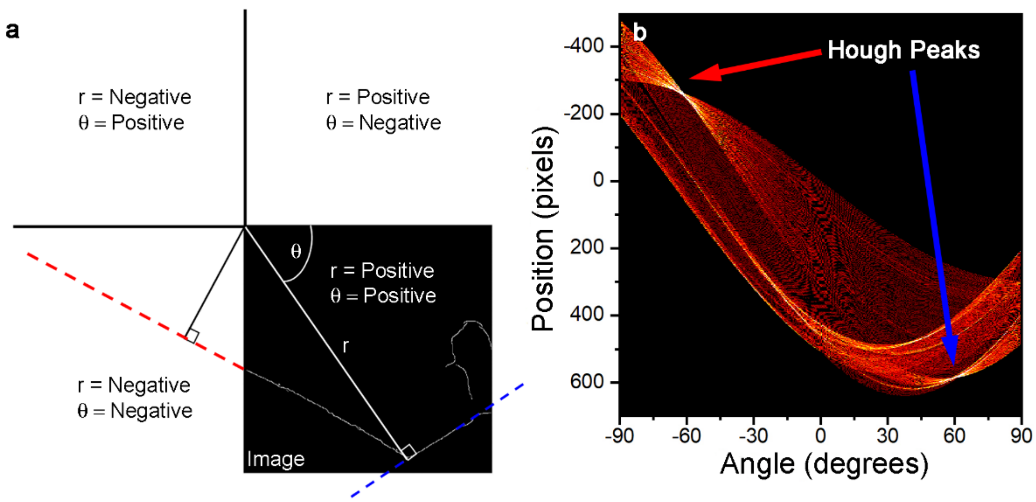

Figure S2. Graphical representation of the Hough transform method. (a) An example binary image with the dashed red and blue lines showing two extended edges. For the blue line, a perpendicular vector with length (r) and angle (θ) is defined. (b) Plot of pixels from the binary image as a function of angle (θ). Non-zero pixels produce the resulting Hough transform. Linear sets of pixels corresponding to an edge or linear feature in the image produce intersections labeled Hough peaks. Here, the dashed red and blue lines in (a) are labeled with corresponding colored arrows at the resulting Hough peaks.

The UEM images and STEM-HAADF image required a rotation for proper alignment. Figure S3 displays the original and the binary images for each technique, in addition to the resulting Hough transforms. The longest edge was identified for each image and is highlighted by the green arrow. The resulting transformation was a 33° counter-clockwise rotation required to align the images. The thermionic image containing the selected-area aperture location did not require any rotation because the same instrument was used and only translational drift had occurred.

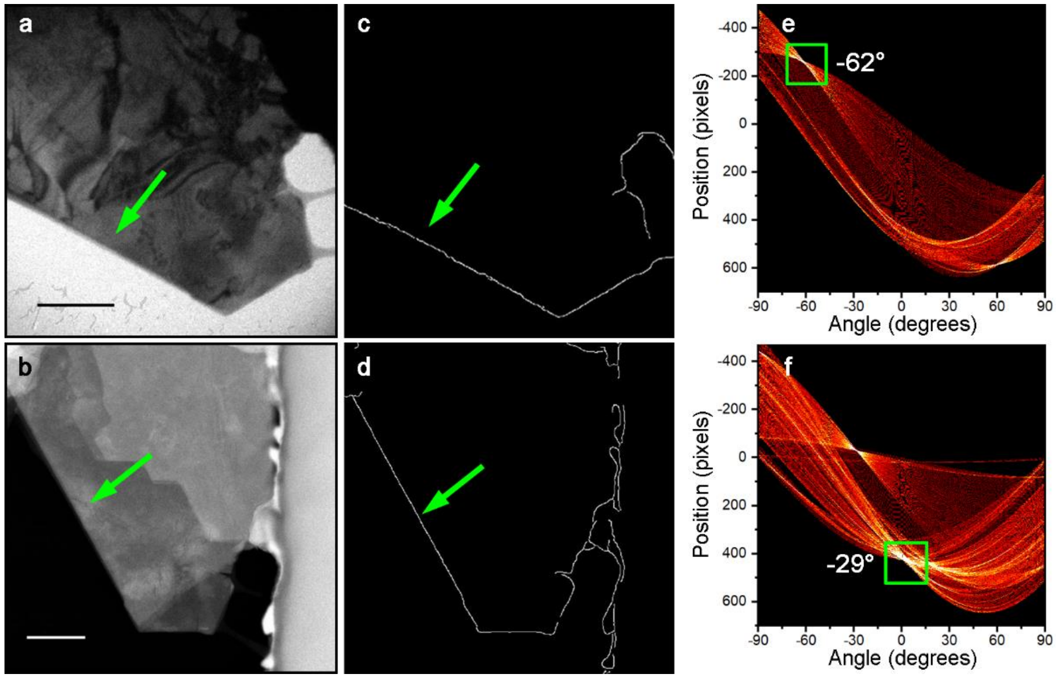

Figure S3. Determination of the relative *xy*-plane orientation of the UEM and HAADF-STEM images. (a,b) UEM bright-field (a) and HAADF-STEM (b) images of the TaS_2 specimen shown in Figures 2 and 3. The green arrows indicate the edge used for alignment. Scale bars represent 1 μm. (c,d) Binary images of each corresponding image created using the Canny method of edge detection. (e,f) Hough transforms with each peak indicated along with the corresponding angle. The difference in the rotation of the edge is 33°.

After applying the rotation, the HAADF-STEM and UEM images were aligned with one another. However, the exact position of each feature within the flake remained offset in the *xy*-plane. Therefore, intersection of the two edges in Figure S3 was used to determine an origin point for each image. The identified positions were offset from one another by 35 pixels in the *x* direction and 78 pixels in the *y* direction. Using the two origin points, the HAADF-STEM image was translated relative to the UEM image to achieve proper alignment (Figure S4). Additionally, the thermionic image was shifted using the template-matching plugin in ImageJ[5] because the contrast was similar enough to identify the correct edge.

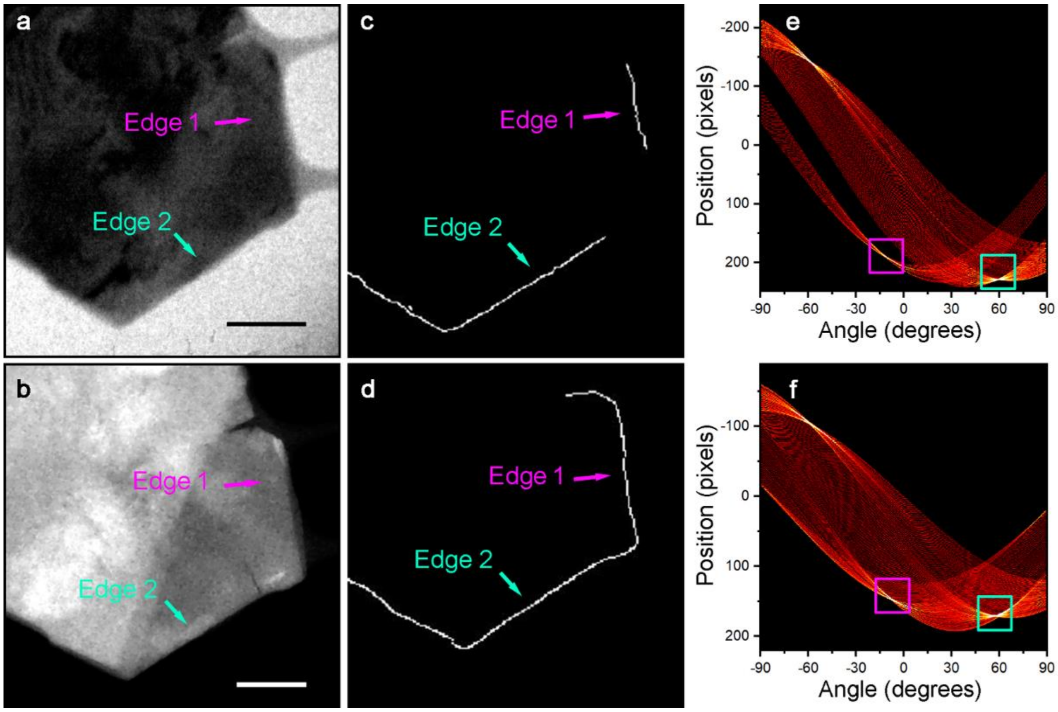

Figure S4. Specimen edge detection for correction of translation in the *xy* image plane. (a,b) Magnified region of the specimen shown in Figure S3 after application of the rotation correction. Two edges used for the shift correction are labeled. Scale bars represent 500 nm. (c,d) Binary images created *via* the Canny edge detection method. (e,f) Hough transforms of each binary image with the peaks for each edge labeled with the corresponding colored squares.

Additionally, the calibration constant for the HAADF-STEM and UEM images were different due to differences in relative camera position for the different instruments and due to slight changes in specimen orientation when transferring between instruments. This was corrected for by tracking the length of several specimen features in each imaging mode and then developing a statistical correlation between each distance. In this way, a calibration ratio of the bright-field to the HAADF-STEM images was used to determine a relative scaling factor of 1.315. This was then applied to the images to match the scales. For example, two features separated by 131.5 pixels in the HAADF-STEM image would be separated by 100 pixels in the UEM image. Following correction, the HAADF-STEM images showing the crystal terrace could be overlaid onto the UEM images in order to identify the position of the feature relative to the analyzed spots BF1 and BF2 shown in Figures 2 and 3. The Hough transform method was also used to identify the location and shape of the terrace within the UEM images (Figure S5). Here, the intersections of each selected edge were used to identify the positions of each discrete section of the terrace. Both the distance and the relative angle of each vector connecting the intersection to the origin was then determined, and the scaling factor was used to scale the vector to the absolute position in the UEM image.

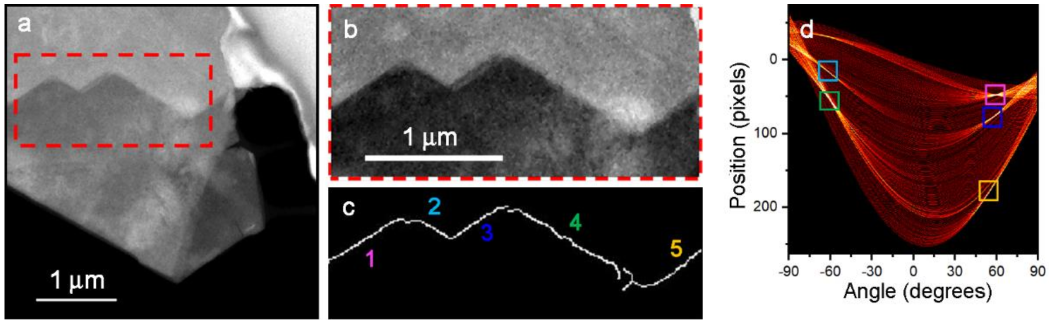

Figure S5. Overlay of the HAADF-STEM image of the crystal terrace onto the UEM bright-field images. (a) HAADF-STEM image of the TaS_2 specimen containing a 26-nm terrace (highlighted with the dashed red rectangle). (b) Magnified region of the terrace section highlighted in (a). (c) Binary image of the terrace in (b), with five identified edges labeled and color coded. (d) The resulting Hough transform containing five peaks labeled and color coded to match the edges in (c).

Finally, in order to identify the location of the selected-area aperture (Figures 2 and 3), separate images of the aperture and the entire flake were acquired after completion of the UEM imaging scan. The selected area was converted to a binary image using edge detection. A circular Hough transform was then used to identify the center and the radius of the aperture relative to the specimen. Because the aperture was acquired over a mask of the bright-field image, the detected center and radius are equal to their exact positions in the UEM image series.

Determination of specimen thickness and *c*-axis acoustic-phonon speed.

Specimen thickness was determined using electron energy-loss spectroscopy (EELS)[6] in scanning mode on an FEI Titan G2 TEM (Thermo Fisher). From the EELS spectra, the absolute thickness can be determined using Equation S1.

$$t = -\lambda \cdot \ln\left(\frac{I_0}{I_p}\right) \qquad \text{(S1)}$$

Here, I_0 and I_p are the intensity of the main beam and the bulk plasmon peak in the spectrum, respectively.[7,8] The mean free path (λ) is calculated from a combination of the average mass of the specimen (Z = 35), the accelerating voltage, the convergent semi-angle (18.2 mrad), and the collection semi-angle (13.89 mrad). In order to find the thickness of the location being analyzed, signal from a region 10 pixels in radius and centered at both BF1 and BF2 was averaged, returning thicknesses of 65.9 ± 5.1 nm and 92.2 ± 9.0 nm, respectively. In these regions, the *c*-axis speeds were calculated using Equation S2.

$$v_c = 2tf_c \qquad \text{(S2)}$$

Here, f_c is the extracted frequency from the UEM bright-field image sequence and t is the measured thickness. From this, the interlayer propagation speeds were calculated to be 3.0 ± 0.2 nm/ps and 3.1 ± 0.2 nm/ps for the 16.3-GHz and 23.9-GHz oscillation frequencies, respectively.

This result is expected for specimen regions having similar elastic constants along the *c*-axis stacking direction.

Determination of basal-plane acoustic-phonon velocity for the specimen in Figures 2 and 3.

The velocity of acoustic mode propagation within the basal plane of the TaS_2 specimen was extracted using a similar method to Figure 1. However, due to spatial confinement, a longer distance was used to extract the velocity. The first observed dynamics at two points separated by 523 nm along the direction of propagation was 110.1 ps correlating to a basal plane velocity of 4.7 ± 0.2 nm/ps. Figure S6a contains the specimen and region at which the intensity was tracked over time. Figure S6b plots the intensity at each time point along the line in Figure S6a for each delay. The time of first intensity oscillation at both distances are tracked by fitting the intensity curve to a baseline and a linear rise/fall. The intersection corresponds to the moment the basal plane strain-waves reach the designated distance which yields the propagation velocity.

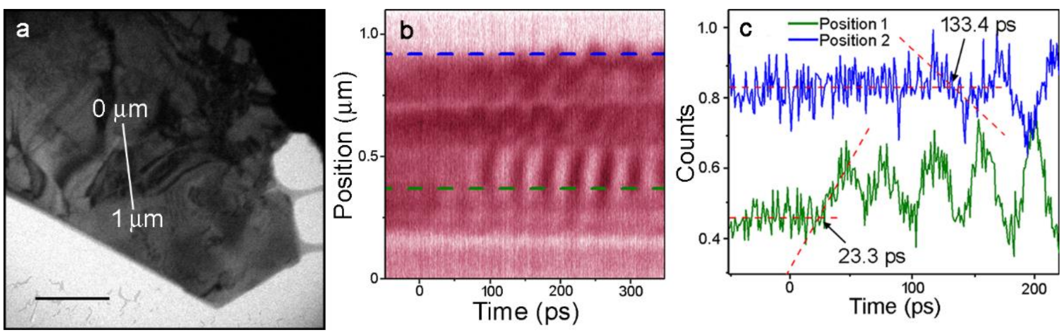

Figure S6. Determination of basal-plane acoustic-phonon velocities *via* generation and analysis of space-time contour plots (STCPs) from UEM image series. (a) Select UEM image of multilayer TaS_2 highlighting the position and length of a 1-µm ROI from which the analysis was performed. (b) STCP generated from the ROI shown in (a). The colored dashed lines mark positions between with which the speed was determined *via* a line profile analysis method. (c) Line profiles generated from the corresponding positions in the STCP in (b). Because the wavefronts are less well-defined than are those shown in Figure S1 and Figure 1, speeds were determined by identifying the moment of onset of observable dynamics in the line profiles (23.3 ± 3.5 ps and 133.4 ± 3.7 ps, intersecting red dashed lines), taking the difference in time (110.1 ± 5.1 ps), and dividing the distance between the two points of interest by the difference in time. This returned an in-plane speed of 4.7 ± 0.2 nm/ps, in reasonably good agreement with the speed determined for the specimen shown in Figures 1 and S1.

References:

1. Cremons, D. R.; Plemmons, D. A.; Flannigan, D. J. Femtosecond electron imaging of defect-modulated phonon dynamics. *Nat. Commun.* **2016**, *7*, 11230.

2. Cremons, D. R.; Plemmons, D. A.; Flannigan, D. J. Defect-mediated phonon dynamics in TaS_2 and WSe_2. *Struct. Dyn.* **2017**, *4*, 044019.

3. McKenna, A. J.; Eliason, J. K.; Flannigan, D. J. Spatiotemporal evolution of coherent elastic strain waves in a single MoS_2 flake. *Nano Lett.* **2017**, *17*, 3952-3958.

4. Zhang, Y.; Flannigan, D. J. Observation of anisotropic strain-wave dynamics and few-layer dephasing in MoS_2 with ultrafast electron microscopy. *Nano Lett.* **2019**, *19*, 8216-8224.

5. Schneider, C. A.; Rasband, W. S.; Eliceiri, K. W. NIH Image to ImageJ: 25 years of image analysis. *Nat. Methods* **2012**, *9*, 671-675.

6. Egerton, R. F.; Cheng, S. C. Measurement of local thickness by electron energy-loss spectroscopy. *Ultramicroscopy* **1987**, *21*, 231-244.

7. Malis, T.; Cheng, S. C.; Egerton, R. F. EELS log-ratio technique for specimen-thickness measurement in the TEM. *J. Electron Microsc. Tech.* **1988**, *8*, 193-200.

8. Tanuma, S.; Powell, C. J.; Penn, D. R. Calculation of electron inelastic mean free paths (IMFPs) VII. Reliability of the TPP-2M IMFP predictive equation. *Surf. Interface Anal.* **2003**, *35*, 268-275.